

# Targetless displacement measurement of RSW based on monocular vision and feature matching

Yong-Soo Ha <sup>1a</sup>, Minh-Vuong Pham <sup>2</sup>, Jeongki Lee <sup>2</sup>, Dae-Ho Yun <sup>2</sup> and Yun-Tae Kim <sup>\*2</sup>

<sup>1</sup> Maritime ICT & Mobility Research Department, Korea Institute of Ocean Science & Technology,  
385, Haeyang-ro, Yeongdo-gu, Busan, Republic of Korea

<sup>2</sup> Department of Ocean Engineering, Pukyong National University, 45, Yongso-ro, Nam-gu, Busan, Republic of Korea

(Received April 28, 2023, Revised September 1, 2023, Accepted October 10, 2023)

**Abstract.** Real-time monitoring of the behavior of reinforced soil retaining wall (RSW) is required for safety checks. In this study, a targetless displacement measurement technology (TDMT) consisting of an image registration module and a displacement calculation module was proposed to monitor the behavior of RSW, in which facing displacement and settlement typically occur. Laboratory and field experiments were conducted to compare the measuring performance of natural target (NT) with the performance of artificial target (AT). Feature count- and location-based performance metrics and displacement calculation performance were analyzed to determine their correlations. The results of laboratory and field experiments showed that the feature location-based performance metric was more relevant to the displacement calculation performance than the feature count-based performance metric. The mean relative errors of the TDMT were less than 1.69 % and 5.50 % for the laboratory and field experiments, respectively. The proposed TDMT can accurately monitor the behavior of RSW for real-time safety checks.

**Keywords:** feature matching; monocular vision; natural target; performance evaluation; reinforced soil retaining wall

## 1. Introduction

Reinforced soil retaining walls (RSWs) have commonly been used worldwide because of their advantages such as cost-effectiveness, easy installation, and versatile design. Most regular safety checks of RSWs are performed periodically through on-site visual inspection. However, it is difficult to predict and prevent the collapse of the RSW using these periodic field surveys. Various measuring sensors, such as laser displacement transducer, strain gauges and earth pressure gauges, were normally installed in the blocks and backfill areas of the RSW to monitor the behavior of RSW (Ling *et al.* 2004, 2009, Weidong *et al.* 2020). However, these devices only provide local measurement results around the measuring device. Therefore, a lot of sensors must be installed to obtain the record for the entire area, which results in high maintenance costs. Recently, in the field of structural health monitoring, various techniques have been developed to measure the displacements and evaluate the stability of the structure. A laser scanner was used to extract geometric characteristics and calculate displacements (Oskouie *et al.* 2016). Total station and laser scanners were applied to measure various monitoring targets (Lienhart 2017). A mobile LiDAR mapping system was proposed to monitor the stability of

RSW using point clouds (Aldosari *et al.* 2020). Remote sensing devices, such as LiDAR and laser scanners, have the advantage of being able to perform overall maintenance through point clouds and three-dimensional (3-D) coordinates. However, owing to the high cost of equipment and a high level of understanding of the remote sensing devices, it is difficult to use them widely in various fields.

Vision-based technology has advantages because of its low price and high usability. In particular, vision-based technologies have the advantage of not only evaluating stability through quantitative analysis but also visually monitoring a site without on-site visits. Various studies have been conducted to measure the behavior of bridges, soil nail walls, retaining walls, and slopes based on 3-D coordinates with images taken from two or more points of view (Jiang and Jauregui 2010, Esmacili *et al.* 2013, Oats *et al.* 2017, Zhao *et al.* 2018). However, since a stereo camera system requires two or more multiple views, two or more cameras must be installed or one camera must be taken from multiple locations. In general, the installation of two or more cameras to monitor one object is not cost effective. Also, when one camera is continuously moved and taken from multiple views, continuous analysis is inefficient because of its additional work. By contrast, the monocular vision takes images and measures displacements from a fixed camera, and this enables continuous measurement. The monocular vision-based monitoring technology contributes to reducing the costs of installation and operation of cameras. Existing cameras such as CCTV, which are widely installed, have the advantage for real-time safety inspections without additional installation. Several

\*Corresponding author, Ph.D., Professor,  
E-mail: yuntkim@pknu.ac.kr

<sup>a</sup> Ph.D., E-mail: ysha@kiost.ac.kr

studies based on monocular vision have been conducted in various areas. In-plane dynamic displacements were analyzed for flexible bridges, masonry specimens, two-story steel frames, and buildings, and the performance of the vision sensor was evaluated (Pan *et al.* 2016, Lee and Shinozuka 2006, Choi *et al.* 2011, Fukuda *et al.* 2013, Feng *et al.* 2015, Liu *et al.* 2021, Wang *et al.* 2021). However, these studies on in-plane displacement have a limitation which is difficult to effectively describe the conditions of structure. In cases where the RSW moves forward (out of a plane), they cannot measure the facing displacement of RSW. These vision-based studies only measured the horizontal and vertical displacements within a plane perpendicular to the camera.

In addition, an artificial target (AT) had to be installed to the region of interest (ROI) to track the target on the structure (Jiang and Jauregui 2010, Esmacili *et al.* 2013, Lee and Shinozuka 2006, Choi *et al.* 2011, Feng *et al.* 2015). However, the AT is not only heterogeneous to the structure, but also it obscures the condition of the structure behind the AT. Therefore, several researches were carried out to measure displacements of structure using a natural target (NT). For example, a specific area such as bolts or nuts in the bridge surface (Pan *et al.* 2016, Fukuda *et al.* 2013) and edge of the structure (Choi *et al.* 2016, Wang *et al.* 2021) is considered as a kind of NT. Choi *et al.* (2016), Wang *et al.* (2021) obtained the displacement by considering the edge of structure as NT. However, these studies used strong references as NTs in order to obtain high performances of detection and matching. In contrast, in RSW, where the simple shape of a block is repeated and stacked, the features of each individual block should be quantitatively evaluated to be used as NT.

The behavior of RSW is caused by the surface load and lateral pressure from the backfill. Various studies have been conducted to determine the general behavior and collapse mechanisms of RSWs. Many researchers have analyzed facing displacement and settlement to figure out the collapse mechanism and the stability of RSWs (Rowe and Skinner 2001, Yoo and Jung 2004, Yoo and Jung 2006, Portelinha *et al.* 2014, Rahardjo *et al.* 2020, Shinde and Mandal 2007, Bathurst and Benjamin 1990, Benjamim *et al.* 2007, Panah *et al.* 2015, Koseki and Hayano 2000, Leonards *et al.* 1994). Koerner and Koerner (2018) analyzed the collapse mechanisms of retaining walls from 320 collapse accidents worldwide. The collapse usually occurred due to facing displacement and settlement caused by the surface load, water pressure, and earth pressure owing to the continuous structural shape of the retaining wall. Therefore, detection and calculation of the facing displacement and settlement for an RSW is most important and necessary to monitor the stability of the RSW. Therefore, in this study, a targetless displacement measurement technology (TDMT) was proposed with an image registration module that detects pixel changes of the RSW block in an image pair and a displacement calculation module that calculates the displacements from the pixel changes. Laboratory and field experiments were conducted to validate the TDMT for the behavior of RSW. The proposed TDMT aims to evaluate monocular vision and

feature matching to analyze the facing displacements and settlements of the RSW blocks using the performance evaluation process through laboratory and field experiments. The goals of this study are as follows: (1) to evaluate whether an RSW block can be used as an NT; (2) to figure out which performance metrics for feature matching are more suitable for displacement calculation; and (3) to evaluate the performance of TDMT for RSW blocks at the laboratory and field scales.

## 2. Targetless displacement measurement technology (TDMT) of RSW

The TDMT includes technologies that detect and match the feature of ROI in an image pair, and calculate the behavior of an RSW based on the pixel change of the target. The terminology ‘targetless’ means that arbitrary RSW blocks are considered as NTs, without artificial target on RSW blocks. Fig. 1 shows the flowchart of the proposed TDMT consisting of an image registration module and displacement calculation module. In the image registration module, feature detection was performed to determine the distribution of features in the ROI sections of the two images before and after the behavior. These detected features of NTs were adapted to match the image pairs. Then the transformation matrix was estimated from the inlier matching features, and the exact pixel coordinate of each NT before and after behavior was figured out. In the displacement calculation module, the pixel changes before and after the behavior were obtained from the changes of pixel coordinates to calculate the displacements using the displacement calculation algorithm.

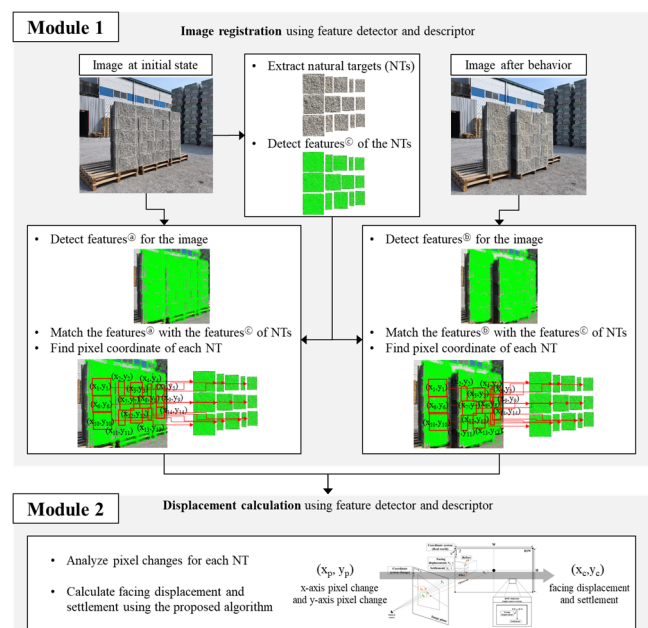


Fig. 1 Flowchart of the proposed TDMT

## 2.1 Image matching

Image-matching methods can be divided into two types: area-based and feature-based. The area-based matching method is typically used for cross-correlation (Avants *et al.* 2008), image correlation (Pan *et al.* 2009), normalized correlation coefficients (Luo and Konofagou 2010), and convolutional neural networks (Haskins *et al.* 2019, Simonovsky *et al.* 2016). However, the target in the image is sometimes covered with small overlapping areas or has large deformations, which are significantly difficult to optimize in similarity measurements. Therefore, the feature-based matching method is widely used in the image-matching community. Since an image can be represented with sparse features, the feature-based matching method is more flexible and robust for matching images with geometric deformation and noise (Jiang *et al.* 2021). Several studies were conducted to determine the optimal feature-matching technique for various types of targets and transformations (Tareen and Saleem 2018, Pieropan *et al.* 2016, Mikolajczyk and Schmid 2005, Chien *et al.* 2016, Ha *et al.* 2022).

In this study, KAZE method, which showed the best matching performance for the behavior of RSW blocks (Ha *et al.* 2022), was used as a feature detector and descriptor to match targets. The KAZE method was developed in nonlinear scale space by means of nonlinear diffusion filtering (Alcantarilla *et al.* 2012). The nonlinear diffusion for an image  $L$  with spatial coordinates and time  $t$  is defined as

$$\frac{\partial L}{\partial t} = \text{div} \left( c(x, y, t) \cdot \nabla L \right), \quad (1)$$

where  $\text{div}$  and  $\nabla$  are respectively the divergence and gradient operators, and  $c$  is a conductivity function. Perona and Malik (1990) proposed a gradient dependent conductivity function  $c$ . The conductivity function  $c$  reduces the diffusion at the location of edge within a region and smooths a region preserving boundaries. The conductivity function  $c$  is defined as

$$c(x, y, t) = g \left( \left| \nabla L_{\sigma} (x, y, t) \right| \right), \quad (2)$$

where the luminance function  $\nabla L_{\sigma}$  is the gradient of a Gaussian smoothed version of the original image  $L$ . The conductivity function  $g$  is chosen to promote wide regions, the conductivity function  $g$  is

$$g = \frac{1}{1 + \frac{|\nabla L_{\sigma}|^2}{k^2}}, \quad (3)$$

where  $k$  is the contrast factor that controls the level of diffusion.

Through this process, the KAZE can make blurring locally adaptive to the image with reducing noise but retaining object boundaries, obtaining superior localization accuracy and distinctiveness (Alcantarilla *et al.* 2012).

Image matching process to track the behavior of the target was performed in the following order: (1) set the ATs and NTs to track the behavior in the image of RSW at the initial state, (2) detect and match features in image pairs (the image of the target at initial state and the image of RSW after the behavior occurred), and (3) estimate the transformation matrix based on inlier matching features. M-estimator sample consensus (MSAC) algorithm with parameters of 100,000 iterations, 99% confidence, and 1.5 maximum distance was used to estimate  $3 \times 3$  transformation matrix from the selected inlier features. The inliers and outliers refer to data in a dataset that is, respectively, consistent with or inconsistent with the underlying pattern in the data. Inliers are data that fit a model well and conform to the trend of the data. For example, in a set of points that form a straight line, the points that are close to the line are considered inliers. Outliers, on the other hand, are data that digress significantly from the rest of the data and do not conform to the general pattern.

### 2.1.1 Performance evaluation

In this study, feature count-based and feature location-based performance metrics were separately analyzed to compare their correlations with the displacement calculation performance. The feature count-based performance metric was obtained through the number of features detected and matched in each image pair. Repeatability and matching score refer to the consistency of a feature detection algorithm in detecting the same features and are widely used to evaluate the matching performance based on the number of features (Mikolajczyk and Mikolajczyk 2004, Revaud *et al.* 2019, Yi *et al.* 2016, Detone *et al.* 2018). Repeatability of each part is the number of matching features divided by the smallest number of features detected in the image pair (Mikolajczyk and Mikolajczyk 2004, Revaud *et al.* 2019)

$$\begin{aligned} &\text{Repeatability} \\ &= \frac{\text{The number of matching features}}{\text{Minimum (the number of detected features)}} \end{aligned} \quad (4)$$

The matching score of each part is the number of inlier matching features divided by the smallest number of features detected in the image pair (Revaud *et al.* 2019, Yi *et al.* 2016, Detone *et al.* 2018)

$$\begin{aligned} &\text{Matching score} \\ &= \frac{\text{The number of inlier matching features}}{\text{Minimum (the number of detected features)}} \end{aligned} \quad (5)$$

The number of inlier matching features indicates the number of features without outlier matching features. However, because feature count-based performance metrics evaluate the performance based on the number of features, it is difficult to quantitatively evaluate the registration of an object in an image before and after matching (Ha *et al.* 2022).

The feature location-based performance metric was obtained through the location of features detected and

matched in each image pair. The mean target registration error (mTRE) is widely used to evaluate the image registration performance in various fields (Chou *et al.* 2013, Rivaz *et al.* 2014, Huizinga *et al.* 2016). In this study, the mTRE was adopted as the feature location-based performance metric. The block image registration error is used to evaluate the quantitative error based on the coordinates of the inlier features in the matched image pair

$$mTRE = \frac{1}{n} \sum_{i=1}^n \sqrt{(x_{ii} - x_{bi})^2 + (y_{ii} - y_{bi})^2} \quad (6)$$

where  $n$  is the number of inlier matching features,  $x_{ti}$  and  $y_{ti}$  are the  $x$  and  $y$  coordinates of each feature in the transformed image, respectively, and  $x_b$  and  $y_b$  are the  $x$  and  $y$  coordinates of each feature in the image after the behavior occurs respectively.

In addition, because mTRE is analyzed based on a specific point within an image pair, its representativeness is imperfect. To compensate for this limitation, the standard deviation of the matching features was analyzed. The standard deviation of the inlier matching features evaluated the distribution of the matching features, which were used as the reference coordinates for mTRE.

## 2.2 Displacement calculation with monocular vision

The facing displacement and settlement, which contribute to the instability of the RSW, are the main safety checkpoints. Therefore, the proposed TDMT was applied to measure two main behaviors (facing displacement and settlement) of RSW using KAZE and displacement calculation algorithm through the images obtained from monocular vision.

### 2.2.1 Displacement calculation algorithm

Fig. 2 compares a stereo camera system with the TDMT. In the stereo camera system,  $P_1$ ,  $P_2$ , and  $P_3$  are points in 3-D space (Fig. 2(a)). It has unclear spatial points (gray zone) from  $P_1$  to  $P_2$  in the left view, and from  $P_2$  to  $P_3$  in the right view. These unclear points can be removed by acquiring images from different viewpoints. Then, 3-D coordinates

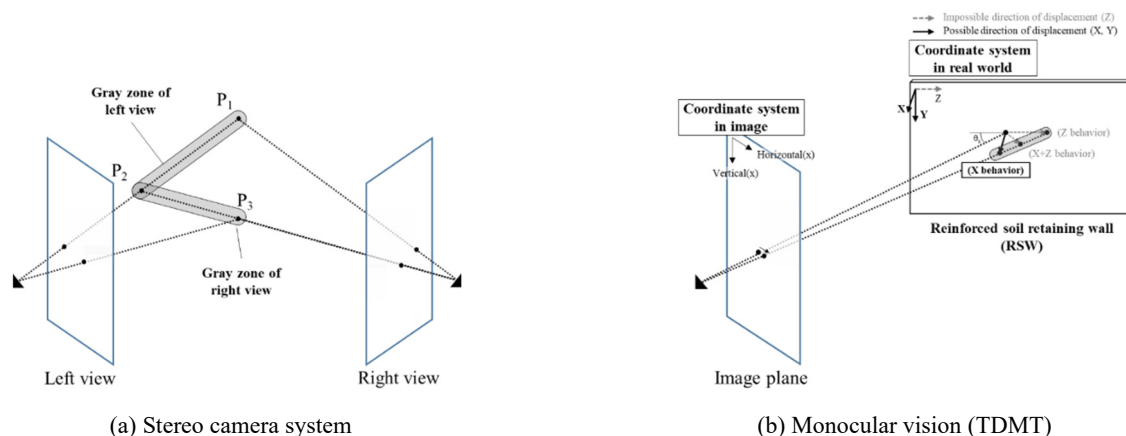


Fig. 2 Comparison of pixel changes in an image with stereo camera system and monocular vision

can be obtained from the depth images. In Fig. 2(b), the behavior in the horizontal direction in an image plane can be normally interpreted as three types of behaviors ( $X$ ,  $X + Z$ , or  $Z$  behaviors in a coordinate system in the real world). However, in the RSW, only facing displacement ( $X$ -direction) and settlement ( $Y$ -direction) occur, and the change in the horizontal direction in the image plane should be interpreted as a displacement in the  $X$ -direction. Furthermore, the change in the vertical direction in the image plane can only be interpreted as a settlement. Therefore, the TDMT with monocularly captured RSW images can be used to clearly measure the behavior of RSWs.

Fig. 3(a) shows a schematic of the displacement calculation process in the TDMT. The calculated facing displacement ( $x_c$ ) and settlement ( $y_c$ ) of the RSW were obtained by computing the  $x$ -axis pixel change ( $x_p$ ) and  $y$ -axis pixel change ( $y_p$ ) in the image plane. Figures 3b and 3c show detailed images to calculate the  $x_c$  and  $y_c$  based on  $x_p$  and  $y_p$ . The pixel changes  $x_p$ ,  $y_p$ , incident angle ( $\theta_x$ ), distance ( $D$ ), and camera parameters (i.e., focal length and pixel size) were used to calculate the displacements ( $x_c$ ,  $y_c$ ).

The process of calculating  $x_c$  through  $x_p$  is as follows. The geometric relationship was calculated using the distance between the camera and center of the RSW.

$$l_0 = D \sin \theta_x, \quad (7)$$

where  $l_0$  is the  $Z$ -axis distance between the camera and center of the RSW.

Through the amount of pixel change in the image, the angles between the points before and after the behaviors and the center of the image are calculated as follows.

$$k_1 = x_e - x_{p1} \quad (8)$$

$$k_2 = x_e - x_{p2} \quad (9)$$

$$\tan \theta_1 = \frac{k_1 \times ps}{f} \quad (10)$$

$$\tan \theta_2 = \frac{k_2 \times ps}{f} \quad (11)$$

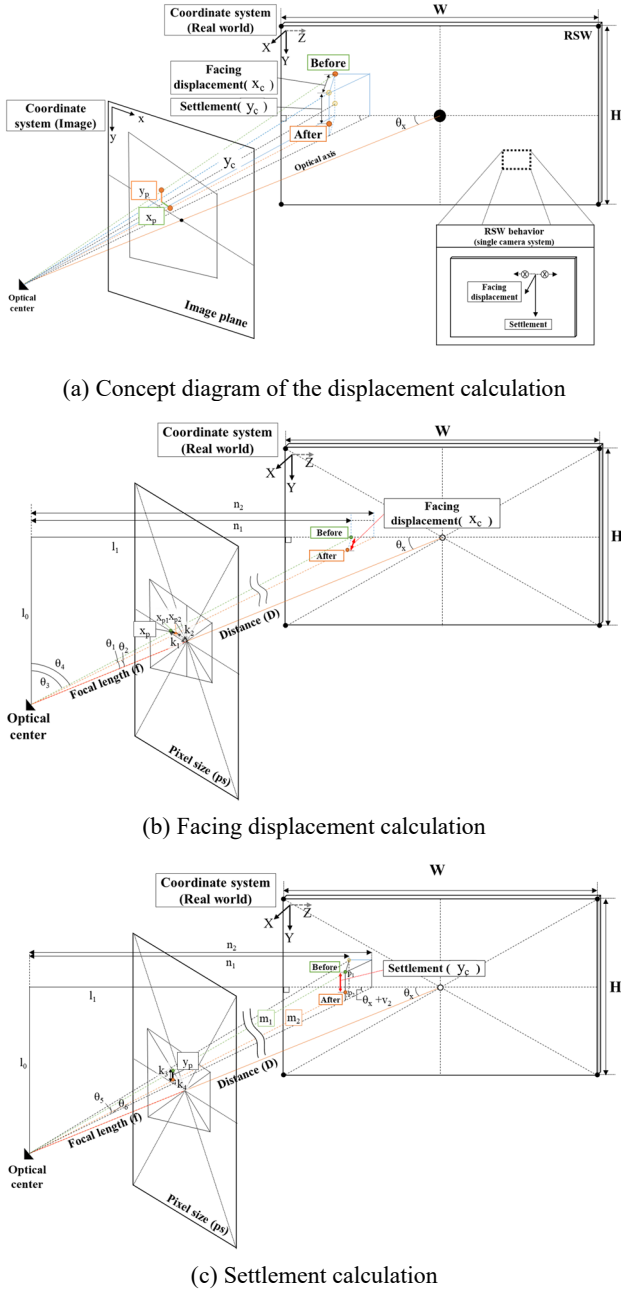


Fig. 3 Schematic diagram of the displacement calculation module in the TDMT.

Here,  $x_c$  is the x-coordinate of the center in the image,  $x_{p1}$  and  $x_{p2}$  are the x-coordinates before and after the behavior of the block, respectively,  $k_1$  and  $k_2$  are the pixel distances on the x-axis from the image center before and after the facing displacement, respectively,  $\theta_1$  and  $\theta_2$  are the angles calculated using  $k_1$  and  $k_2$  from the optical center, respectively,  $ps$  is the pixel size, and  $f$  is the focal length.

The coordinates for the X-axis behavior in the RSW were calculated, and the facing displacement ( $x_c$ ) was obtained using the following equations.

$$\theta_3 = \frac{\pi}{2} - (\theta_x + \theta_1) \quad (12)$$

$$\theta_4 = \frac{\pi}{2} - (\theta_x + \theta_2) \quad (13)$$

$$n_1 = l_0 \times \tan\theta_3 \quad (14)$$

$$n_2 = l_0 \times \tan\theta_4 \quad (15)$$

$$x_c = (l_0 \times \tan\theta_4 - l_0 \times \tan\theta_3) \times \tan(\theta_x + \theta_2) \quad (16)$$

Fig. 3(c) shows the schematic of the settlement calculation. The process of calculating the settlement  $y_c$  using  $y_p$  is as follows. The distances between the optical center and the points before and after settlement were calculated as follows

$$m_1 = \frac{l_0}{\cos\theta_3}, \quad (17)$$

$$m_2 = \frac{l_0}{\cos\theta_4} - \frac{n_2 - n_1}{\cos(\theta_4 + \theta_2)} \quad (18)$$

where  $m_1$  and  $m_2$  are the distances between the optical center and the initial point and the point after settlement occurred, respectively.

The angles between the points before and after the behaviors and the center of the image are calculated as follows.

$$k_3 = y_e - y_{p1} \quad (19)$$

$$k_4 = y_e - y_{p2} \quad (20)$$

$$\tan\theta_5 = \frac{k_3}{f} \quad (21)$$

$$\tan\theta_6 = \frac{k_4}{f} \quad (22)$$

Here,  $y_c$  is the y-coordinate of the center in the image,  $y_{p1}$  and  $y_{p2}$  are the y-coordinates before and after the behavior of the block, respectively,  $k_3$  and  $k_4$  are the pixel distances on the y-axis from the image center before and after settlement in the image, respectively, and  $\theta_5$  and  $\theta_6$  are the angles calculated using  $k_3$  and  $k_4$  from the optical center, respectively.

The coordinate for the Y-axis behavior in the RSW is calculated, and the settlement ( $y_c$ ) is obtained through the following equations.

$$p_1 = m_1 \times \tan\theta_5 \quad (23)$$

$$p_2 = m_2 \times \tan\theta_6 \quad (24)$$

$$y_c = p_2 - p_1 \quad (25)$$

Here,  $p_1$  and  $p_2$  are the Y-coordinates of the objects before and after settlement, respectively.

The error and mean relative error (MRE) were used to evaluate the displacement calculation performance by comparing the calculated and reference displacements. Each performance metric for the displacement calculation was analyzed based on the Euclidean distance without

separately calculating the facing displacement and settlement. The MRE was only analyzed for the parts where the facing displacement and settlement occurred because the reference displacement was used as the denominator in the MRE. The MRE was calculated by averaging  $MRE_x$  and  $MRE_y$  using Eqs. (23)-(25).

$$MRE_x(\%) = \frac{1}{m} \sum_{i=1}^m \left| \frac{x_{ci} - x_{ri}}{x_{ri}} \right| \times 100, \quad (26)$$

$$MRE_y(\%) = \frac{1}{m} \sum_{i=1}^m \left| \frac{y_{ci} - y_{ri}}{y_{ri}} \right| \times 100, \quad (27)$$

$$MRE(\%) = \frac{MRE_x + MRE_y}{2}, \quad (28)$$

where  $x_c$  and  $y_c$  are the calculated facing displacement and settlement using TDMT, respectively.  $x_r$  and  $y_r$  are the reference facing displacement and settlement measured from the total station, respectively, and  $m$  is the number of targets.

### 2.2.2 Validation of the displacement calculation algorithm

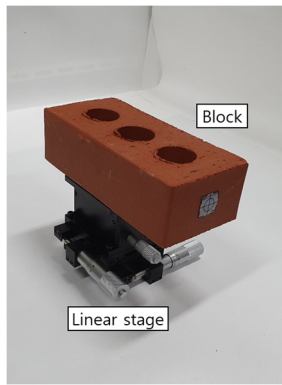
Fig. 4 shows the experimental setup of the pilot-phase experiment constructed to verify the displacement calculation algorithm. The facing displacement, settlement, and combined displacement (facing displacement + settlement) of a block were generated to be 10 mm each using

a linear stage (Fig. 4(a)). The displacement was analyzed using images taken at incident angles between  $5^\circ$  and  $85^\circ$  with the experimental set up (Fig. 4(b)). As shown in Fig. 4(c), the distance and incident angle were measured. The distances for each incident angles were similarly distributed in range of 745 to 793 mm. KAZE was used to match and calculate the pixel changes of the block before and after the behaviors. Images taken at a low incident angle of  $5 - 15^\circ$  were excluded because the facing of the block was not sufficiently photographed, and the features could not be sufficiently detected and matched.

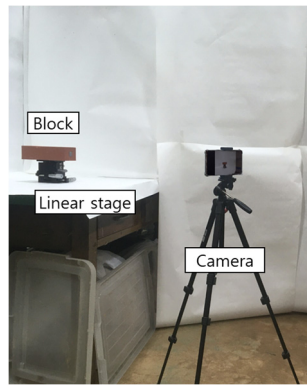
Moreover, images taken at a high incident angle of  $75 - 85^\circ$  had difficulty capturing the behavior because they provided almost no change in pixels. Therefore, it is recommended to analyze the image at incident angles of  $20 - 70^\circ$ . Table 1 lists the results of the pilot-phase experiment. The displacement calculation performance was evaluated by comparing the results of the displacement calculation algorithm with input displacements. The error was distributed from 0.07 mm to 0.49 mm, and the RMSE was 0.36 mm in the incident angle from  $20^\circ$  to  $70^\circ$ . The results indicated that the displacement calculated using the proposed algorithm was in good agreement with the reference displacement.

## 3. Experiments

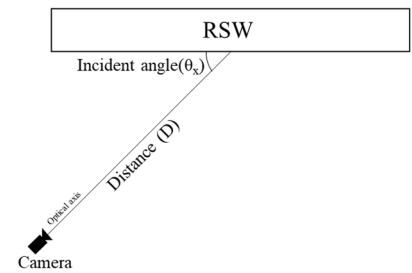
Two types of RSW experiments, laboratory and field,



(a) Block and linear stage that generates precise behavior



(b) Experimental setup of camera



(c) Top view of incident angle and distance of the experiment

Fig. 4 Pilot-phase experiment for validation of the TDMT

Table 1 Results of pilot-phase experiment

Repetition	Incident angle ( $\theta_x, ^\circ$ )	Error (mm)			Minimum error (mm)	Maximum error (mm)	RMSE (mm)
		Horizontal	Vertical	Average			
10	20	0.49	0.46	0.47	0.07	0.49	0.36
	30	0.45	0.40	0.43			
	40	0.13	0.47	0.30			
	50	0.14	0.41	0.28			
	60	0.07	0.46	0.27			
	70	0.30	0.16	0.23			

Table 2 RSW block size in the laboratory and field experiments

Type	Model	Specifications
Laboratory RSW block	-	Height: 30 mm, Width: 50 mm, Length: 35 mm
Field RSW block	G1	Height: 250 mm, Width: 500 mm, Length: 430 mm

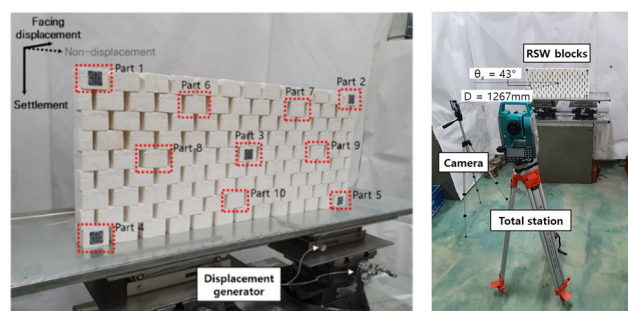
Table 3 Description of the camera and total station

Type	Model	Specifications
Camera	SM-G977N	Image sensor: Samsung SAK2LD, 4032×3024 resolution Pixel size: 1.8 $\mu\text{m}$ , Focal length: 5.4 mm
Total station	Sokkia SET510K	Accuracy: 1–3 mm

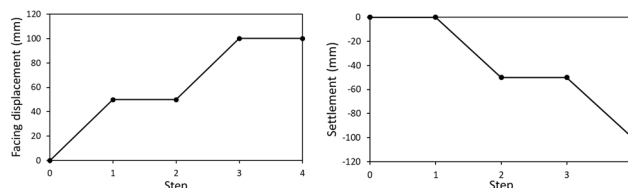
were conducted to evaluate the image-matching and displacement calculation performances. In this study, the matching and displacement calculation performance at each position in the RSW was evaluated using the proposed monocular vision-based TDMT. We took several parts to detect and calculate the displacement for each experiment in order to evaluate performance according to the distance from the camera to each target within the image. Also, features were detected and matched to targets with high accuracy even if the distance becomes larger, since feature matching methods were measured up to 7 decimal places (ten millionths). Therefore, the performance with different distances from the camera to RSW was not considered. The general behavior was simulated for all blocks of RSW in the laboratory experiment and for specific blocks of the RSW in the field experiment. Table 2 presents a description of the laboratory and the field RSW blocks. The laboratory RSW block had a scale of 1:10 in the block standard (KS F 4416), and the blocks were made by injecting gypsum into a block mold. G1 RSW blocks, which are widely used in domestic RSW construction sites, were used for the field experiment. Table 3 shows a description of the camera and total station. The total station used had an accuracy of 1–3 mm. The measured result of the total station was used as the reference displacement.

### 3.1 Laboratory experiment

The laboratory experiment was performed preferentially to evaluate the matching and displacement calculation performances under controlled conditions in a laboratory environment. Fig. 5(a) shows an experimental RSW (width: 650 mm, height: 270 mm) made of 121 blocks, as shown in Table 2. The sheet targets were attached to 5 blocks of RSW to measure the behaviors of blocks using a total station and considered as ATs. Fig. 5(b) shows the experimental setup, consisting of RSW blocks, a camera, and a total station. The camera was installed at a position ( $\theta_x = 43^\circ$ ,  $D = 1,267$  mm) in the range of incident angles ( $20 - 70^\circ$ ) suggested through the pilot-phase experiment. Four steps of facing displace-



(a) Monitoring targets for detection and tracking behavior (b) Experimental setup of camera and total station



(c) Facing displacement and settlement with step-by-step behavior

Fig. 5 Details of laboratory experiments

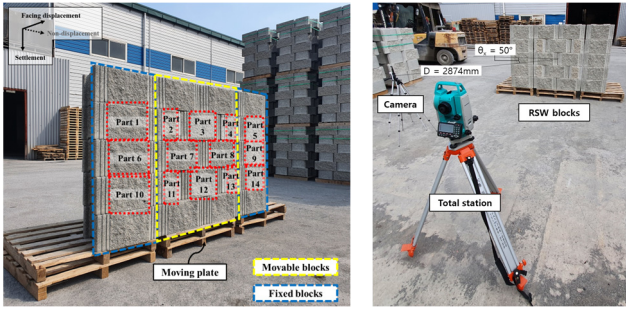
ment and settlement were generated step by step using the displacement generator under the RSW (Fig. 5(c)).

The displacements were calculated by matching and analyzing the images of the evenly distributed 10 target blocks (red boxes in Fig. 5(a)) taken before and after the behaviors. Image matching and displacement calculation were performed for 5 ATs and 5 NTs. The matching performance was evaluated based on repeatability, matching score, number of inlier matching features, and mTRE. The displacement calculation performance was evaluated by comparing the reference displacements which were measured from the total station. In addition, the correlation between the performance of matching and displacement calculation was analyzed.

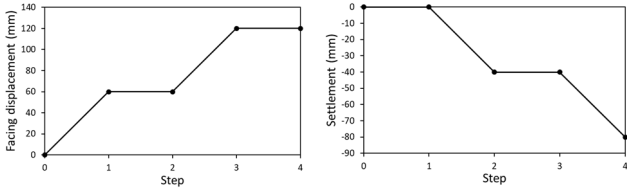
### 3.2 Field experiment

A field experiment was conducted to evaluate the displacement calculation performance under field conditions. Fig. 6 shows the experimental setup. The RSW (width = 2,000 mm, height = 1,250 mm) consisted of 22 blocks that are widely used in construction sites (Fig. 6(a)). The RSW blocks are divided into movable and fixed blocks. The facing displacement and settlement of the movable blocks (yellow box in Fig. 6(a)) were generated step by step using a moving plate (Fig. 6(c)). The left and right boundary blocks did not move during the experiment (blue box in Fig. 6(a)). The camera was installed at a position ( $\theta_x = 50^\circ$ ,  $D = 2,874$  mm) in the range of incident angles suggested through the pilot-phase experiment.

The sheet targets were attached to each center of the nine blocks (Parts 1-9) and used as a reference point for the total station measurement. The displacements of the 14 targets (red boxes in Fig. 6(a)) in the RSW were calculated by analyzing the images taken before and after displacement generation. In the field experiment, all targets were considered as NTs because the size of the sheet target



(a) Field RSW blocks and monitoring targets for detecting and tracking behavior (b) Experimental setup of camera and total station



(c) Facing displacement and settlement with step-by-step behavior  
Fig. 6 Details of field experiments

was small and did not significantly affect the matching of blocks. The experimental process of the matching and displacement calculation performances were evaluated in the same way as in the laboratory experiment, and the correlation between the matching and displacement calculation performances was also analyzed.

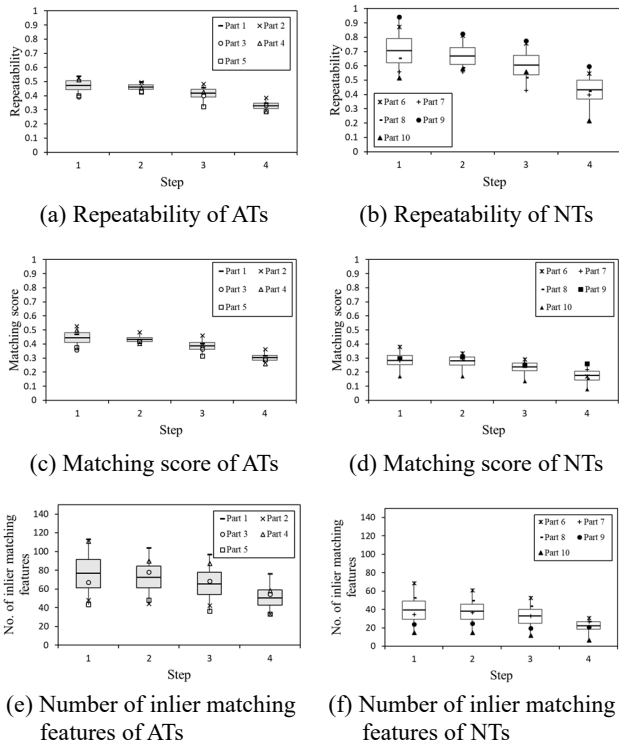


Fig. 7 Count-based performance metrics in laboratory experiments

## 4. Experimental results and discussions

### 4.1 Laboratory experiment

Fig. 7 shows the feature count-based performance metrics such as repeatability, matching score, and number of matching features in the laboratory experiment. The matching performances were evaluated for the ATs (1 - 5 parts) and the NTs (6 - 10 parts). Gray and white boxes in Fig. 7 represents the mean and standard deviation of ATs and NTs, respectively. All metrics slightly decreased as the steps progressed (i.e., facing displacement and settlement occurred with the step in Fig. 5(c)). NTs have higher repeatability with more features being matched than ATs. However, a large number of outlier matching features of NTs were excluded from the MSAC algorithm, and significantly fewer inlier matching features were selected to estimate the transformation matrix than that of ATs. Therefore, a ratio of inlier matching features of NTs was smaller, and the matching efficiency was relatively lower than that of ATs.

Fig. 8 shows the feature location-based performance metrics. As the steps progressed, the feature location-based metrics in terms of mTRE (Figs. 8(a), (b)) and standard deviation (Figs. 8(c), (d)) increased, which means that the matching performance decreased. The mTRE and standard deviation of NTs were similar to those of ATs.

Fig. 9 presents the results of the calculated and reference facing displacements and settlements in the laboratory experiment. The results showed that the calculated displacements agreed well with the reference displacements, although there were minor errors (Figs. 9(a) and (b)). The displacement error was distributed from 0.09 mm to 1.89 mm at ATs and from 0.11 mm to 1.68 mm at NTs (Figs. 9(c) and (d)). The displacement error results indicated that the performance decreased as the steps progressed, there was no significant difference in errors between NTs and ATs. The displacement calculation performances were more related to the feature count-based performance metrics,

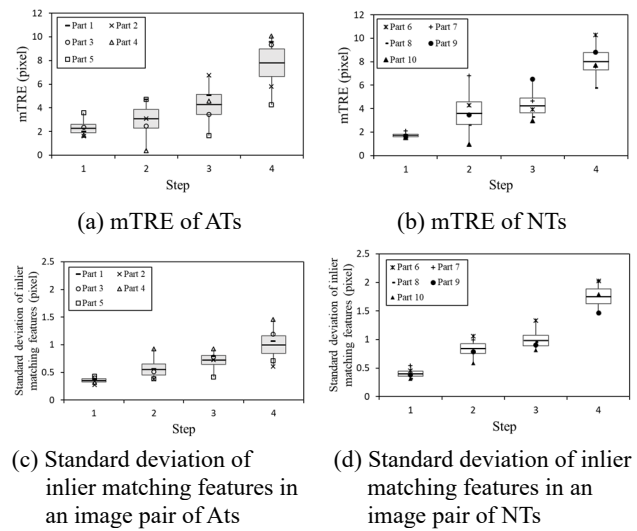


Fig. 8 Location-based performance metrics in laboratory experiments

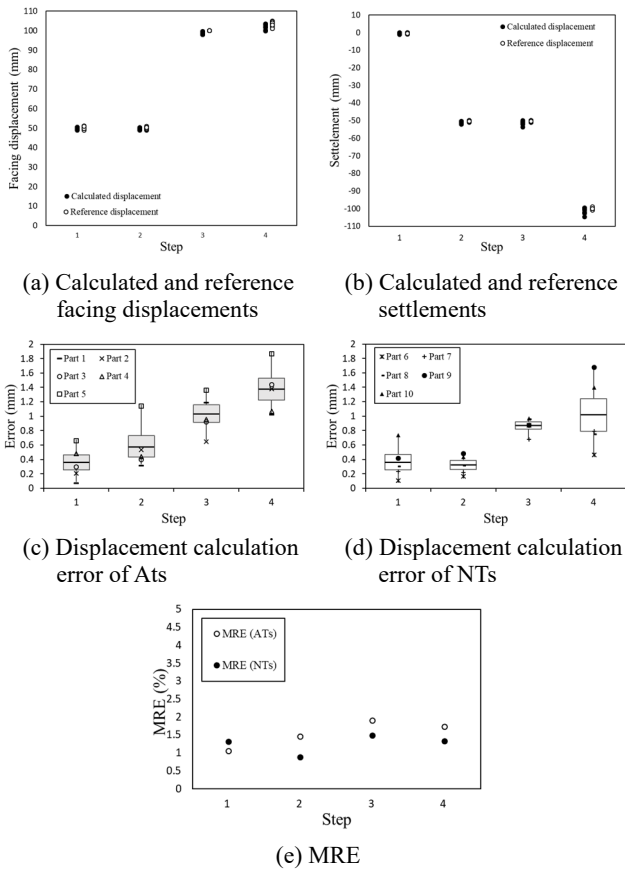


Fig. 9 Results of the laboratory experiments

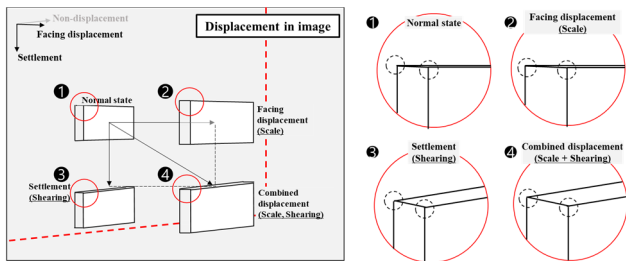


Fig. 10 Examples of the block shape according to the behavior of the block in the image

indicating that feature location-based performance metrics were more robust metrics to explain matching performance. In addition, the RSW blocks can be used as NTs.

The MRE was distributed without significant fluctuations regardless of the progress of the stage, and the MRE ranged from 0.87% to 1.9%, with an average of 1.53% for ATs and 1.24% for NTs (Fig. 9(d)). Fig. 10 presents examples of the block shapes in the image according to the facing displacement, settlement, and combined displacement. As the steps progressed, scale and shear transformations continued to occur, which increased the complexity of the transformation in the image-matching procedure. Therefore, both displacement calculation errors increased and the matching performance decreased as the facing displacement and settlement of the RSW occurred cumulatively.

## 4.2 Field experiment

Fig. 11 shows the feature count-based performance metrics of both the movable and fixed blocks for the field experiment. The repeatability and matching scores of the movable blocks were slightly lower than those of the fixed blocks. The number of inlier matching features also showed lower performance in the movable blocks than in the fixed

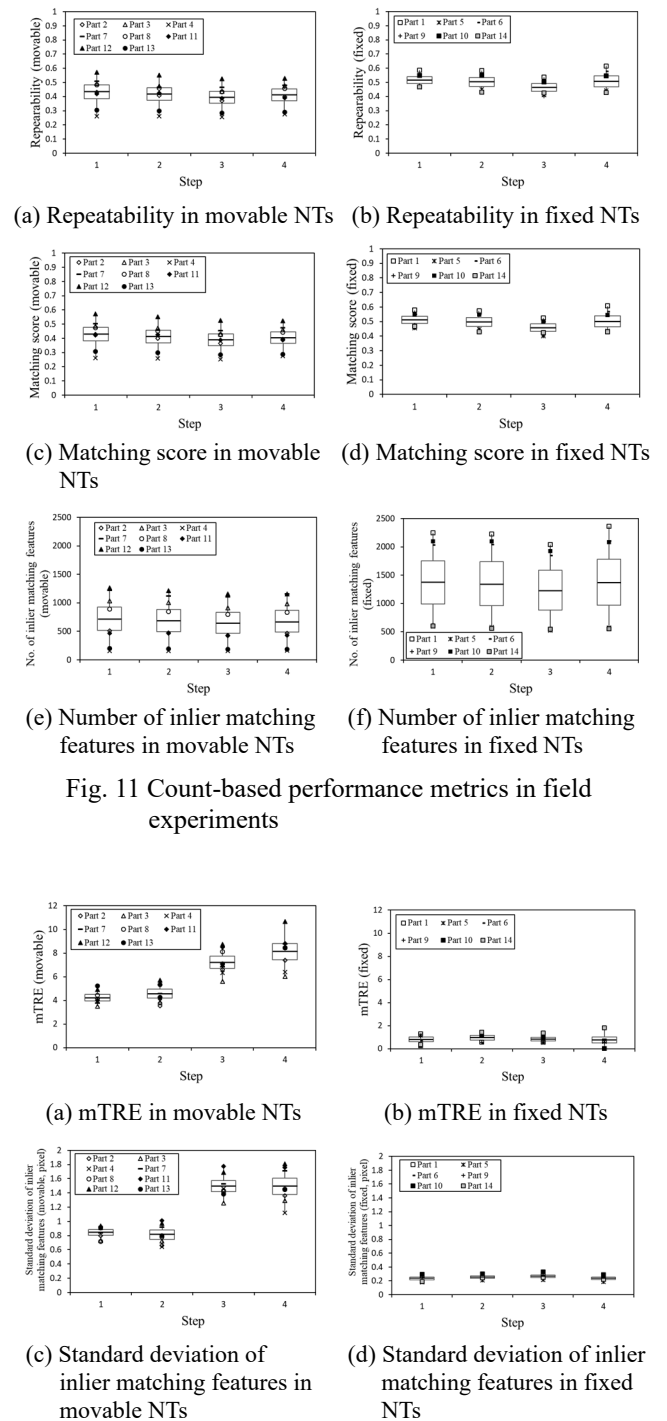


Fig. 11 Count-based performance metrics in field experiments

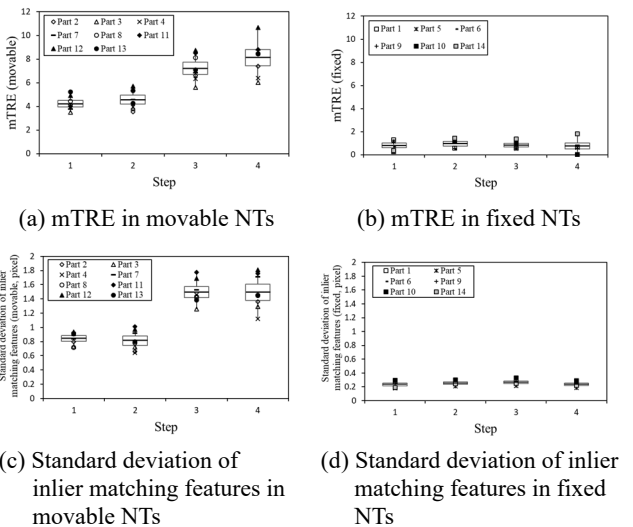


Fig. 12 Location-based performance metrics in field experiments

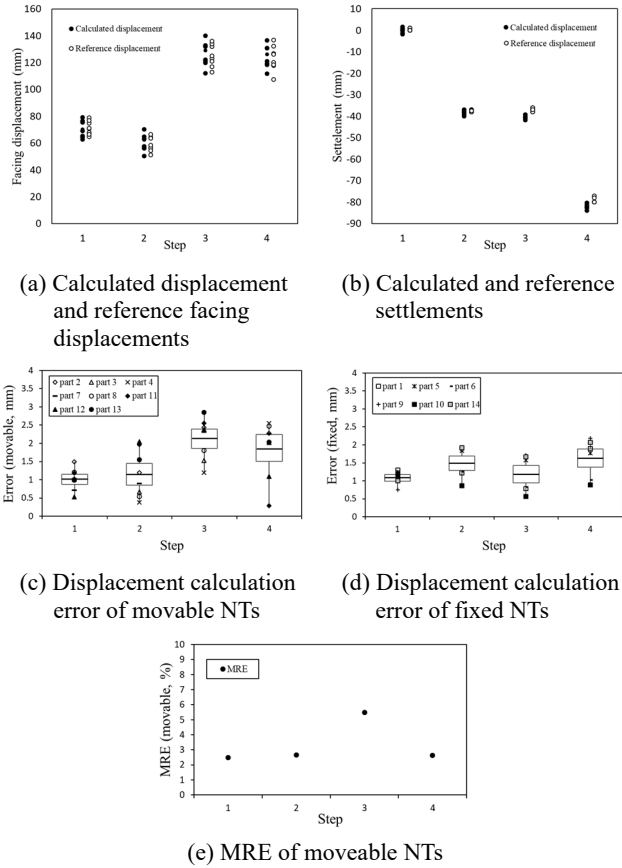


Fig. 13 Results of field experiments

blocks because the transformation induced after the behavior significantly affects the image registration. In the movable and fixed blocks, the feature count-based performance metrics were not significantly changed as the steps progressed. Fig. 12 shows the feature location-based performance metrics of both the movable and fixed blocks for the field experiments. Feature location-based performance metrics such as mTRE and standard deviation of inlier matching features tended to increase in the movable blocks as the steps progressed. However, there were no significant changes in the fixed blocks according to step progress (Figs. 12(b) and (d)).

Figs. 13(a) and (b) show the calculated and reference facing displacements and settlements, respectively, for the movable blocks in the field experiments. The calculated behaviors agreed with the reference behaviors, although minor errors occurred in some parts. Figs. 13(c) and (d) show the displacement calculation error for the field experiment. In particular, the trend of errors in the movable and fixed blocks increased as the steps progressed (Figs. 13(c) and (d)). This shows a similar trend to the feature location-based performance metrics (Figs. 12(a) and (b)) rather than the trend of the feature count-based performance metrics (Figs. 11(a), (c) and (e)). This implies that the feature location-based performance metrics provide more accurate results than the feature count-based performance metrics when quantitatively evaluating the matching performance for image registration. Therefore, feature location-based performance metrics are preferentially

recommended to evaluate the image matching performance in the field.

The displacement calculation errors were distributed in range of 0.29 mm to 2.85 mm for the movable blocks and 0.56 mm to 2.18 mm for the fixed blocks. In addition, for the movable blocks, the MRE ranged from 2.48% to 5.48%, with an average of 3.31%. The field experiments also indicated that each block of RSW can be considered as an NT.

## 5. Conclusions

In this study, the TDMT was proposed to analyze the behavior of RSWs. Based on the results of the pilot-phase experiment, laboratory and field RSW experiments were conducted to evaluate the performance of the proposed TDMT.

In the laboratory experiment, the repeatability of NTs was greater than that of ATs, but the matching score and number of inlier matching features of NTs were smaller than those of ATs, resulting in inconsistency for feature count-based performance metrics (repeatability, matching score, and the number of inlier matching features). On the other hand, feature location-based performance metrics (mTRE and standard deviation of inlier matching features) and displacement calculation performance of NTs were similar to those of ATs. Based on performance results, it is found that the performance of NT is similar to that of AT, and each block of RSW can be used as an NT.

In the field experiment, the feature location-based performance metrics and displacement calculation performance decreased as the steps progressed. However, the feature count-based performance metrics were not significantly changed as the steps progressed, since the feature count-based performance metrics were not affected by the displacements. Therefore, the feature location-based performance metrics were more suitable to accurately evaluate the displacement calculation performance.

Regarding to displacement calculation performance, the maximum displacement calculation errors were less than 1.89 mm and 2.85 mm in laboratory and field experiments, respectively. The average MREs were 1.39% and 3.31% in the laboratory and field experiments, respectively, which shows excellent displacement calculation performance to measure typical behavior of RSW. The proposed TDMT can be used to quantitatively measure the behavior of the RSW, in which each RSW block is considered as an NT.

Although the proposed approach obtained great performance in measuring displacement of the RSW, the proposed technique focused on the matching and displacement calculation performances for the limited behavior of blocks occurring in laboratory and field RSW. In future studies, the performance of matching and displacement calculations for different conditions such as various incident angles and distances, and various displacement types such as bulging and overturning, which commonly occur in RSWs, should be evaluated. Additionally, various field conditions such as changes in weather and brightness should be taken into account for a comprehensive analysis.

## Acknowledgments

This research was supported by Korea Institute of Marine Science & Technology Promotion (KIMST) funded by the Ministry of Oceans and Fisheries, Korea (20210659), and a Technology Innovation Program (Grant K-G012001951201) funded by the Ministry of Trade, Industry & Energy (MOTIE, Korea).

## References

- Alcantarilla, P.F., Bartoli, A. and Davison, A.J. (2012), "KAZE features", In: *Computer Vision—ECCV 2012: 12th European Conference on Computer Vision*, Florence, Italy, October, pp. 214-227.
- Aldosari, M., Al-Rawabdeh, A., Bullock, D. and Habib, A. (2020), "A mobile LiDAR for monitoring mechanically stabilized earth walls with textured precast concrete panels", *Remote Sens.*, **12**, 306. <https://doi.org/10.3390/rs12020306>
- Avants, B.B., Epstein, C.L., Grossman, M. and Gee, J.C. (2008), "Symmetric diffeomorphic image registration with cross-correlation: evaluating automated labeling of elderly and neurodegenerative brain", *Med. Image Anal.*, **12**, 26-41. <https://doi.org/10.1016/j.media.2007.06.004>
- Bathurst, R.J. and Benjamin, D.J. (1990), "Failure of a geogrid-reinforced soil wall", *Transp. Res. Rec.*, **1288**, 109-116.
- Benjamin, C., Bueno, B. and Zornberg, J.G. (2007), "Field monitoring evaluation of geotextile-reinforced soil-retaining walls", *Geosynth. Int.*, **14**, 100-118. <https://doi.org/10.1680/gein.2007.14.2.100>
- Chien, H.J., Chuang, C.C., Chen, C.Y. and Klette, R. (2016), "When to Use What Feature? SIFT, SURF, ORB, or A-KAZE Features for Monocular Visual Odometry", *Proceedings of the IEEE International Conference on Image and Vision Computing*, Palmerston North, New Zealand, November, pp. 1-6. <https://doi.org/10.1109/IVCNZ.2016.7804434>
- Choi, H.S., Cheung, J.H., Kim, S.H. and Ahn, J.H. (2011), "Structural dynamic displacement vision system using digital image processing", *NDT & E Int.*, **44**, 597-608. <https://doi.org/10.1016/j.ndteint.2011.06.003>
- Choi, I., Kim, J. and Kim, D. (2016), "A target-less vision-based displacement sensor based on image convex hull optimization for measuring the dynamic response of building structures", *Sensors*, **16**, 2085. <https://doi.org/10.3390/s16122085>
- Chou, C.R., Frederick, B., Mageras, G., Chang, S. and Pizer, S. (2013), "2D/3D image registration using regression learning", *Comput. Vis. Image Underst.*, **117**, 1095-1106. <https://doi.org/10.1016/j.cviu.2013.02.009>
- DeTone, D., Malisiewicz, T. and Rabinovich, A. (2018), "Superpoint: Self-supervised interest point detection and description", *Proceedings of the IEEE Conference on Computer Vision and Pattern Recognition Workshops*, Salt Lake City, UT, USA, June, pp. 224-236. <https://doi.org/10.1109/CVPRW.2018.00060>
- Esmaili, F., Varshosaz, M. and Ebadi, H. (2013), "Displacement measurement of the soil nail walls by using close range photogrammetry and introduction of CPDA method", *Meas.*, **46**, 3449-3459. <https://doi.org/10.1016/j.measurement.2013.04.069>
- Feng, D., Feng, M.Q., Ozer, E. and Fukuda, Y. (2015), "A vision-based sensor for noncontact structural displacement measurement", *Sens.*, **15**, 16557-16575. <https://doi.org/10.3390/s150716557>
- Fukuda, Y., Feng, M.Q., Narita, Y., Kaneko, S.I. and Tanaka, T. (2013), "Vision-based displacement sensor for monitoring dynamic response using robust object search algorithm", *IEEE Sens. J.*, **13**, 4725-4732. <https://doi.org/10.1109/JSEN.2013.2273309>
- Ha, Y.S., Lee, J. and Kim, Y.T. (2022), "Performance Evaluation of Feature Matching Techniques for Detecting Reinforced Soil Retaining Wall Displacement", *Remote Sens.*, **14**, 1697. <https://doi.org/10.3390/rs14071697>
- Haskins, G., Kruecker, J., Kruger, U., Xu, S., Pinto, P.A., Wood, B.J. and Yan, P. (2019), "Learning deep similarity metric for 3D MR-TRUS image registration", *Int. J. Comput. Assist. Radiol. Surg.*, **14**, 417-425. <https://doi.org/10.1007/s11548-018-1875-7>
- Huizinga, W., Poot, D.H., Guyader, J.M., Klaassen, R., Coolen, B.F., van Kranenburg, M., Van Geuns, R.J.M., Uitterdijk, A., Polfliet, M., Vandemeulebroucke, J. and Leemans, A. (2016), "PCA-based groupwise image registration for quantitative MRP", *Medical Image Anal.*, **29**, 65-78. <https://doi.org/10.1016/j.media.2015.12.004>
- Jiang, R. and Jauregui, D.V. (2010), "Development of a digital close-range photogrammetric bridge deflection measurement system", *Meas.*, **43**, 1431-1438. <https://doi.org/10.1016/j.measurement.2010.08.015>
- Jiang, X., Ma, J., Xiao, G., Shao, Z. and Guo, X. (2021), "A review of multimodal image matching: Methods and applications", *Inform. Fusion*, **73**, 22-71. <https://doi.org/10.1016/j.inffus.2021.02.012>
- Koerner, R.M. and Koerner, G.R. (2018), "An Extended Data Base and Recommendations Regarding 320 Failed Geosynthetic Reinforced Mechanically Stabilized Earth (MSE) Walls", *Geotext. Geomembr.*, **46**, 904-912. <https://doi.org/10.1016/j.geotextmem.2018.07.013>
- Koseki, J. and Hayano, K. (2000), "Preliminary report on damage to retaining walls caused by the 1999 Chi-Chi earthquake", *Bulletin of ERS*, **33**, 23-34.
- Lee, J.J. and Shinozuka, M. (2006), "Real-time displacement measurement of a flexible bridge using digital image processing techniques", *Exp. Mech.*, **46**, 105-114. <https://doi.org/10.1007/s11340-006-6124-2>
- Leonards, G.A., Frost, J.D. and Bray, J.D. (1994), "Collapse of geogrid-reinforced retaining structure", *J. Perform. Constr. Facil.*, **8**, 274-292. [https://doi.org/10.1061/\(ASCE\)0887-3828\(1994\)8:4\(274\)](https://doi.org/10.1061/(ASCE)0887-3828(1994)8:4(274))
- Lienhart, W. (2017), "Geotechnical monitoring using total stations and laser scanners: critical aspects and solutions", *J. Civil Struct. Health Monit.*, **7**, 315-324. <https://doi.org/10.1007/s13349-017-0228-5>
- Ling, H.I., Liu, H., Kaliakin, V.N. and Leshchinsky, D. (2004), "Analyzing dynamic behavior of geosynthetic-reinforced soil retaining walls", *J. Eng. Mech.*, **130**, 911. [https://doi.org/10.1061/\(ASCE\)0733-9399\(2004\)130:8\(911\)](https://doi.org/10.1061/(ASCE)0733-9399(2004)130:8(911))
- Ling, H.I., Leshchinsky, D., Wang, J.P., Mohri, Y. and Rosen, A. (2009), "Seismic response of geocell retaining walls: experimental studies", *J. Geotech. Geoenv. Eng.*, **135**, 515-524. [https://doi.org/10.1061/\(ASCE\)1090-0241\(2009\)135:4\(515\)](https://doi.org/10.1061/(ASCE)1090-0241(2009)135:4(515))
- Liu, D., Tang, Z., Bao, Y. and Li, H. (2021), "Machine-learning-based methods for output-only structural modal identification", *Struct. Control Health Monitor.*, **28**(12), e2843. <https://doi.org/10.1002/stc.2843>
- Luo, J. and Konofagou, E.E. (2010), "A fast normalized cross-correlation calculation method for motion estimation", *IEEE Trans. Ultrason. Ferroelectr. Freq. Control*, **57**, 1347-1357. <https://doi.org/10.1109/TUFFC.2010.1554>
- Mikolajczyk, K. and Mikolajczyk, K. (2004), "Scale & Affine Invariant Interest Point Detectors", *Int. J. Comput. Vis.*, **60**, 63-86. <https://doi.org/10.1023/B:VISI.0000027790.02288>
- Mikolajczyk, K. and Schmid, C. (2005), "A performance evaluation of local descriptors", *IEEE Trans. Pattern Anal. Mach. Intell.*, **27**, 1615-1630.

- <https://doi.org/10.1109/TPAMI.2005.188>  
Oats, R.C., Escobar-Wolf, R. and Oommen, T. (2017), "A novel application of photogrammetry for retaining wall assessment", *Infrastruct.*, **2**, 10.  
<https://doi.org/10.3390/infrastructures2030010>
- Oskouie, P., Becerik-Gerber, B. and Soibelman, L. (2016), "Automated measurement of highway retaining wall displacements using terrestrial laser scanners", *Autom. Constr.*, **65**, 86-101. <https://doi.org/10.1016/j.autcon.2015.12.023>
- Pan, B., Qian, K., Xie, H. and Asundi, A. (2009), "Two-dimensional digital image correlation for in-plane displacement and strain measurement: a review", *Meas. Sci. Technol.*, **20**, 062001. <https://doi.org/10.1088/0957-0233/20/6/062001>
- Pan, B., Tian, L. and Song, X. (2016), "Real-time, non-contact and targetless measurement of vertical deflection of bridges using off-axis digital image correlation", *Ndt & E Int.*, **79**, 73-80. <https://doi.org/10.1016/j.ndteint.2015.12.006>
- Panah, A.K. and Yazdi, M. and Ghalandarzadeh, A. (2015), "Shaking table tests on soil retaining walls reinforced by polymeric strips", *Geotext. Geomembr.*, **43**, 148-161. <https://doi.org/10.1016/j.geotexmem.2015.01.001>
- Perona, P. and Malik, J. (1990), "Scale-space and edge detection using anisotropic diffusion", *IEEE Transact. Pattern Anal. Mach. Intell.*, **12**, 629-639. <https://doi.org/10.1109/34.56205>
- Pieropan, A., Bjorkman, M., Bergstrom, N. and Kragic, D. (2016), "Feature descriptors for tracking by detection: A benchmark", arXiv 2016, arXiv:1607.06178. <https://doi.org/10.48550/arXiv.1607.06178>
- Portelinha, F.H.M., Zornberg, J.G. and Pimentel, V. (2014), "Field performance of retaining walls reinforced with woven and nonwoven geotextiles", *Geosynthe. Int.*, **21**, 270-284. <https://doi.org/10.1680/gein.14.00014>
- Rahardjo, H., Kim, Y., Gofar, N. and Satyanaga, A. (2020), "Analyses and design of steep slope with GeoBarrier system (GBS) under heavy rainfall", *Geotext. Geomembr.*, **48**, 157-169. <https://doi.org/10.1016/j.geotexmem.2019.11.010>
- Revaud, J., Weinzapfel, P., de Souza C.R., Pion, N., Csurka, G., Cabon, Y. and Humenberger, M. (2019), "R2D2: repeatable and reliable detector and descriptor", arXiv 2019, arXiv:1906.06195. <https://doi.org/10.48550/arXiv.1906.06195>
- Rivaz, H., Karimaghloo, Z. and Collins, D.L. (2014), "Self-similarity weighted mutual information: a new nonrigid image registration metric", *Med. Image Anal.*, **18**, 343-358. <https://doi.org/10.1016/j.media.2013.12.003>
- Rowe, R.K. and Skinner G.D. (2001), "Numerical analysis of geosynthetic reinforced retaining wall constructed on a layered soil foundation", *Geotext. Geomembr.*, **19**, 387-412. [https://doi.org/10.1016/S0266-1144\(01\)00014-0](https://doi.org/10.1016/S0266-1144(01)00014-0)
- Shinde, A.L. and Mandal, J.N. (2007), "Behavior of reinforced soil retaining wall with limited fill zone parameter", *Geotechn. Geol. Eng.*, **25**, 657-672. <https://doi.org/10.1007/s10706-007-9138-3>
- Simonovsky, M., Gutiérrez-Becker, B., Mateus, D., Navab, N. and Komodakis, N. (2016), "A deep metric for multimodal registration", *Proceedings of the International Conference on Medical Image Computing and Computer-Assisted Intervention*, pp. 10-18.
- Tareen, S.A.K. and Saleem, Z.A. (2018), "Comparative Analysis of SIFT, SURF, KAZE, AKAZE, ORB, and BRISK", *Proceedings of the 2018 IEEE International Conference on Computing, Mathematics and Engineering Technologies (iCoMET)*, Sukkur, Pakistan, March, pp. 1-10. <https://doi.org/10.1109/ICOMET.2018.8346440>
- Wang, J., Zhao, J., Liu, Y. and Shan, J. (2021), "Vision-based displacement and joint rotation tracking of frame structure using feature mix with single consumer-grade camera", *Struct. Control Health Monit.*, **28**, e2832. <https://doi.org/10.1002/stc.2832>
- Weidong, H., Xinnian, Z., Xiaohong, L., Yongqing, Z. and Xiyu, Z. (2020), "Active earth pressure against cantilever retaining wall adjacent to existing basement exterior wall", *Int. J. Geomech.*, **20**, 04020207. [https://doi.org/10.1061/\(ASCE\)GM.1943-5622.000185](https://doi.org/10.1061/(ASCE)GM.1943-5622.000185)
- Yi, K.M., Trulls, E., Lepetit, V. and Fua, P. (2016), "Lift: Learned Invariant Feature Transform", In: *European Conference on Computer Vision*, Cham, Switzerland, pp. 467-483. [https://doi.org/10.1007/978-3-319-46466-4\\_28](https://doi.org/10.1007/978-3-319-46466-4_28)
- Yoo, C. and Jung, H.S. (2004), "Measured behavior of a geosynthetic-reinforced segmental retaining wall in a tiered configuration", *Geotext. Geomembr.*, **22**, 359-376. [https://doi.org/10.1016/S0266-1144\(03\)00064-5](https://doi.org/10.1016/S0266-1144(03)00064-5)
- Yoo, C. and Jung, H.Y. (2006), "Case history of geosynthetic reinforced segmental retaining wall failure", *J. Geotech. Geoenviron. Eng.*, **132**, 1538-1548. [https://doi.org/10.1061/\(ASCE\)1090-0241\(2006\)132:12\(1538\)](https://doi.org/10.1061/(ASCE)1090-0241(2006)132:12(1538))
- Zhao, S., Kang, F. and Li, J. (2018), "Displacement monitoring for slope stability evaluation based on binocular vision systems", *Optik*, **171**, 658-671. <https://doi.org/10.1016/j.ijleo.2018.06.097>

HJ